

# Transformation of the Excited State and Photovoltaic Efficiency of $\text{CH}_3\text{NH}_3\text{PbI}_3$ Perovskite upon Controlled Exposure to Humidified Air

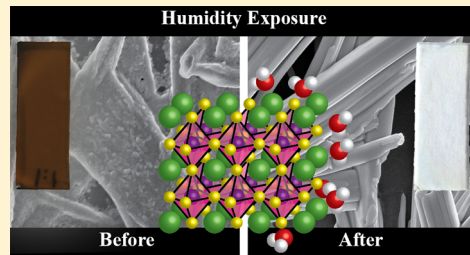
Jeffrey A. Christians,<sup>†,‡</sup> Pierre A. Miranda Herrera,<sup>†,||</sup> and Prashant V. Kamat\*,<sup>†,‡,§</sup>

<sup>†</sup>Radiation Laboratory, <sup>‡</sup>Department of Chemical and Biomolecular Engineering, and <sup>§</sup>Department of Chemistry and Biochemistry, University of Notre Dame, Notre Dame, Indiana 46556, United States

<sup>||</sup>Department of Chemical and Biotechnological Engineering, Instituto Tecnológico y de Estudios Superiores de Monterrey, Atizapán de Zaragoza, Estado de México, 52926 Mexico

## S Supporting Information

**ABSTRACT:** Humidity has been an important factor, in both negative and positive ways, in the development of perovskite solar cells and will prove critical in the push to commercialize this exciting new photovoltaic technology. The interaction between  $\text{CH}_3\text{NH}_3\text{PbI}_3$  and  $\text{H}_2\text{O}$  vapor is investigated by characterizing the ground-state and excited-state optical absorption properties and probing morphology and crystal structure. These undertakings reveal that  $\text{H}_2\text{O}$  exposure does not simply cause  $\text{CH}_3\text{NH}_3\text{PbI}_3$  to revert to  $\text{PbI}_2$ . It is shown that, in the dark,  $\text{H}_2\text{O}$  is able to complex with the perovskite, forming a hydrate product similar to  $(\text{CH}_3\text{NH}_3)_4\text{PbI}_6 \cdot 2\text{H}_2\text{O}$ . This causes a decrease in absorption across the visible region of the spectrum and a distinct change in the crystal structure of the material. Femtosecond transient absorption spectroscopic measurements show the effect that humidity has on the ultrafast excited state dynamics of  $\text{CH}_3\text{NH}_3\text{PbI}_3$ . More importantly, the deleterious effects of humidity on complete solar cells, specifically on photovoltaic efficiency and stability, are explored in the light of these spectroscopic understandings.



## INTRODUCTION

The unprecedented rise in the efficiency of organic–inorganic lead halide perovskite solar cells witnessed over the past few years has captured the attention of the greater scientific community. The National Renewable Energy Laboratory (NREL) recently certified a perovskite solar cell with efficiency in excess of 20% (<http://www.nrel.gov/ncpv/>), and they seem primed to surpass the efficiency of many proven commercial photovoltaic (PV) technologies.<sup>1</sup> Contrary to current commercial PV technologies, perovskite solar cells can be simply manufactured using low-temperature, solution-based methods. This gives them potential use in building facades, as a top cell in a Si–perovskite tandem architecture, as an “all-perovskite” multijunction solar cell, or simply as an inexpensive single junction solar cell.<sup>2–4</sup> In spite of the great progress in efficiency over the past several years, perovskite solar cells exhibit significant degradation in performance even over time periods as short as days or weeks.<sup>5–7</sup> For commercial applications, especially if used in conjunction with Si solar cells as a tandem device, operating lifetimes of 20–30 years are desired. A better understanding of this degradation in performance is critical to controlling these processes and developing perovskite solar cells that are suitable for real world commercial applications.

Specifically, the effect of atmospheric humidity on  $\text{CH}_3\text{NH}_3\text{PbI}_3$  is of interest due to its role in the degradation of the performance of perovskite solar cell.<sup>6,7</sup> To avoid exposure to humidity during solar cell fabrication, nearly all groups carry out perovskite deposition in a dry atmosphere and take pains to avoid exposure to humidity following device

fabrication. We have experienced this first hand in our research on perovskite solar cells, where our solar cells fabricated in high relative humidity (RH) conditions (>50% RH) have shown much reduced PV performance compared to those made under dry conditions. On the other hand, Zhou et al. recently reported that exposure to a low level of humidity (30% RH) during solar cell fabrication controlled the perovskite crystal formation, which aided them in boosting the power conversion efficiency to 19.3%,<sup>8</sup> and Bass et al. demonstrated how humidity can facilitate crystallization.<sup>9</sup> Snaith and co-workers recently suggested that using P3HT/SWNTs-PMMA as the hole transport medium (HTM) can provide improved thermal stability and resistance to moisture,<sup>10</sup> and Smith et al. showed that moisture stability could be improved by substituting  $\text{C}_6\text{H}_5(\text{CH}_2)_2\text{NH}_3$  for  $\text{CH}_3\text{NH}_3$ .<sup>11</sup> Finally, in our own work, we have found that using an inorganic HTM in place of spiro-OMeTAD can provide improved stability in ambient conditions.<sup>5</sup> Thus, the effects of humidity exposure on the methylammonium lead iodide necessitate a closer look.

In this study, we investigate the transformation undergone by  $\text{CH}_3\text{NH}_3\text{PbI}_3$  upon humidity exposure. We provide a detailed look into the changes manifest in the optical absorption, film morphology, crystal structure, and excited state dynamics when perovskite films are exposed to different atmospheric conditions in the dark. This offers the most complete picture to date of the mechanism of degradation under  $\text{H}_2\text{O}$  exposure and elucidates

Received: November 3, 2014

Published: January 15, 2015



several interesting features of the perovskite. Lastly, we explored the stability of perovskite solar cells stored at 0%, 50%, and 90% RH, in order to characterize how the PV performance is affected by humidity. These results show a comprehensive picture of the changes undergone by  $\text{CH}_3\text{NH}_3\text{PbI}_3$  when exposed to water vapor and its relation to PV performance.

## ■ EXPERIMENTAL SECTION

**Materials.** 2-Propanol (IPA, Sigma-Aldrich, anhydrous, 99.5%), 4-*tert*-butylpyridine (Sigma-Aldrich, 96%), alumina nanoparticles (Sigma-Aldrich, <50 nm particle size, 20 wt % in IPA), chlorobenzene (Alfa Aesar, 99.5%), FK 102 Co(III) TFSI salt ( $\text{Co}[\text{PyPz}]_3[\text{TFSI}]_3$ , Dyesol), lithium bis(trifluoromethanesulfonimide) (LiTFSI, Sigma-Aldrich, 99.95%), lead iodide ( $\text{PbI}_2$ , Sigma-Aldrich, 99.999%), methylammonium iodide ( $\text{CH}_3\text{NH}_3\text{I}$ , Dyesol), *N,N*-dimethylformamide (DMF, Sigma-Aldrich, anhydrous, 99.8%), spiro-OMeTAD (Merck), titanium diisopropoxide bis(acetylacetone) (TAA, Sigma-Aldrich, 75 wt % in IPA), zinc powder (median 6–9  $\mu\text{m}$ , Alfa Aesar, 97.5%), and all other chemicals were used as received without further purification.

**Perovskite Films.** Glass slides were cleaned by sonication in a 2% Hellmanex solution for 15 min followed by rinses with DI  $\text{H}_2\text{O}$  and EtOH and cleaning in an air plasma for 5 min. A 4 wt % solution of  $\text{Al}_2\text{O}_3$  nanoparticles in IPA was spin-coated onto the cleaned glass slides at 6000 rpm for 30 s to form a mesoporous scaffold. The films were then dried at 150 °C for 30 min. Next, a 1:1 mol ratio mixture of  $\text{CH}_3\text{NH}_3\text{I}$  and  $\text{PbI}_2$  was dissolved at 200 mg mL<sup>-1</sup> in DMF by stirring at 70 °C. This solution was then spin-cast onto the  $\text{Al}_2\text{O}_3$  films at 2000 rpm for 30 s and annealed at 70 °C for 30 min to form  $\text{CH}_3\text{NH}_3\text{PbI}_3$  films. The same procedure was used to obtain a  $\text{PbI}_2$  control sample, except that the solution used was 200 mg mL<sup>-1</sup>  $\text{PbI}_2$  dissolved in DMF. For XRD measurements, a 40 wt % equimolar solution of  $\text{CH}_3\text{NH}_3\text{I}$  and  $\text{PbI}_2$  in DMF was used to maximize the signal-to-noise ratio.

PEDOT:PSS substrates were used for the planar perovskite films employed in SEM characterization. For these films, PEDOT:PSS was diluted 1:3 in IPA, sonicated for 15 min at room temperature, spin-coated onto cleaned glass slides at 2000 rpm for 30 s, and finally dried at 150 °C for 30 min. The films were preheated to 70 °C prior to spin-coating the perovskite precursor solution to improve surface coverage. In all cases perovskite deposition was carried out in a moisture-free glovebox.

**$\text{CH}_3\text{NH}_3\text{PbI}_3$  Hydrate Synthesis.** The  $\text{CH}_3\text{NH}_3\text{PbI}_3$  hydrate was synthesized by following a previously reported procedure for the synthesis of  $(\text{CH}_3\text{NH}_3)_4\text{PbI}_6 \cdot 2\text{H}_2\text{O}$ .<sup>12</sup> In this synthesis, 1 mL of aqueous 0.2 M  $\text{Pb}(\text{NO}_3)_2$  was added dropwise to 5 mL of aqueous 1.2 M  $\text{CH}_3\text{NH}_3\text{I}$  at room temperature. A bright yellow precipitate was formed instantaneously upon the addition of  $\text{Pb}(\text{NO}_3)_2$ . This precipitate was allowed to stand in contact with the mother liquor overnight, by which time the yellow solid had fully converted to pale yellow crystals. A video depicting this transformation is included in the Supporting Information. These crystals were then dried by vacuum filtration and then were characterized by powder XRD.

**Relative Humidity Control.** For all the humidity studies, the perovskite films were stored at room temperature (measured as 23 ± 1 °C) in the dark in 500 mL controlled-humidity chambers. The relative humidity in the chambers was attenuated to the desired humidity ±5% by a water/glycerol solution with careful adjustment of the water to glycerol ratio.<sup>13</sup> The precise relative humidity was measured periodically throughout the course of the experiments using a calibrated hygrometer. The chambers were only opened when necessary, typically once per day or less, and generally required less than 30 min to reach their equilibrium humidity as measured using a hygrometer.

**Solar Cell Fabrication.** Perovskite solar cells were fabricated using a procedure similar to that employed previously by other research groups.<sup>14,15</sup> FTO glass (Pilkington Glass, TEC-7, 2 mm thickness) was cleaned as described above. A compact  $\text{TiO}_2$  layer was deposited by

spin-coating a 0.15 M solution of TAA in 1-butanol. The films were dried for 10 min at 125 °C following the deposition, and a ~150 nm mesoporous  $\text{TiO}_2$  layer was cast on top of the compact layer by spin-coating a diluted  $\text{TiO}_2$  paste (~40 nm particles). The films were then annealed at 500 °C for 1 h. The  $\text{TiO}_2$  films were stored following this annealing step until needed.

The mesoporous films were treated in aqueous 20 mM  $\text{TiCl}_4$  at 90 °C for 10 min, rinsed with DI  $\text{H}_2\text{O}$  and EtOH, dried, and annealed at 500 °C for 30 min. The perovskite layer was then formed via a sequential deposition method. For this, a 1 M  $\text{PbI}_2$  solution in DMF was made by stirring and heating the solution at 70 °C for 30 min. The  $\text{PbI}_2$  was deposited on the mesoporous  $\text{TiO}_2$  substrate by spin-coating at 5000 rpm for 20 s and dried on a hot plate at 40 °C for 3 min followed by 100 °C for 5 min. The dry  $\text{PbI}_2$  films were then converted to  $\text{CH}_3\text{NH}_3\text{PbI}_3$  by immersion in 8 mg mL<sup>-1</sup>  $\text{CH}_3\text{NH}_3\text{I}$  solution in IPA for 20 s followed by drying of perovskite film at 100 °C for 5 min. The spiro-OMeTAD hole conductor was deposited by spin-coating at 5000 rpm for 30 s from a chlorobenzene solution containing 72.3 mg mL<sup>-1</sup> spiro-OMeTAD, 28.8  $\mu\text{L}$  mL<sup>-1</sup> 4-*tert*-butylpyridine, 17.5  $\mu\text{L}$  mL<sup>-1</sup> of LiTFSI stock solution (stock: 520 mg mL<sup>-1</sup> LiTFSI in acetonitrile), and 26.3  $\mu\text{L}$  mL<sup>-1</sup> of FK 102 Co(III) TFSI stock solution (stock: 300 mg mL<sup>-1</sup> FK102 in acetonitrile). After hole conductor deposition, the films were stored overnight in dry air and were then completed by the evaporation of a 100 nm layer of Au, which forms the back contact of the solar cell.

**Characterization.** UV-visible absorption measurements were conducted using a Varian Cary 50 Bio spectrophotometer. Images of the film morphology were obtained using an FEI Magellan-400 field emission scanning electron microscope (FESEM) operated at 5 keV. X-ray diffraction measurements were conducted with a Bruker D8 Advance Davinci powder X-ray diffractometer using a Cu  $\text{K}\alpha$  source, a standard step size of 0.02°, and an acquisition time of 400 s deg<sup>-1</sup>. Perovskite films on mesoporous  $\text{Al}_2\text{O}_3$  substrates were mounted without further modification. Photoelectrochemical measurements were carried out using a Princeton Applied Research 2273 (PARstat) potentiostat. The solar cells were tested under 100 mW cm<sup>-2</sup> AM 1.5G simulated solar irradiation from a 300 W Xe lamp coupled with an AM 1.5 filter. Incident photon to current efficiencies (IPCE) were measured using a Newport/Oriel measurement system with a calibrated silicon photodiode for reference.

**Femtosecond Transient Absorption.** Femtosecond transient absorption measurements of  $\text{CH}_3\text{NH}_3\text{PbI}_3$  films on  $\text{Al}_2\text{O}_3$  were conducted using a Clark MXR 2010 (775 nm, 1 mJ pulse<sup>-1</sup>, fwhm pulse width = 130 fs, 1 kHz repetition rate) and an Ultrafast Systems (Helios) UV-visible detection system. The fundamental laser output was split into pump (95%) and probe (5%) beams. The pump beam was directed through a second harmonic frequency doubler to produce the 387 nm pump beam, and the probe beam was passed through an optical delay rail and focused on a Ti:sapphire crystal to produce a white light continuum. The pump was attenuated at 8  $\mu\text{J}$  pulse<sup>-1</sup> and the optical delay stage provided a probe time window of 1.6 ns. Kinetic traces were assembled at the appropriate wavelengths from the time-resolved spectral data. All films studied were placed in evacuated quartz cells for measurement.

## ■ RESULTS AND DISCUSSION

**UV–Visible Absorption.** The perovskite crystal structure, shown in Figure 1, can be described by the general formula ABX<sub>3</sub>, where A and B are cations and X is an anion. In the case of the organic–inorganic hybrid perovskites in photovoltaics, the prototypical compound has been  $\text{CH}_3\text{NH}_3\text{PbI}_3$ . More generally though, A is an organic cation (typically  $\text{RNH}_3^+$ ), X is a halogen, and B is a divalent metal (almost exclusively Pb for photovoltaics, although sometimes Sn as well).<sup>16</sup> Looking more closely at the crystal structure of these organic–inorganic hybrid perovskites, these crystals are held together by ionic interactions between the organic and inorganic portion as well

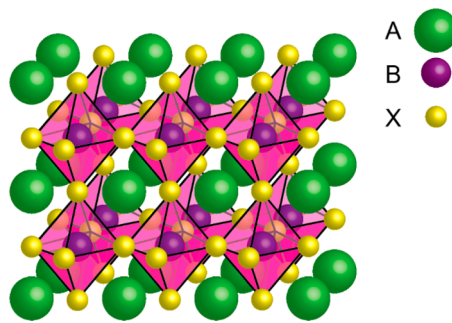


**Figure 1.** Scheme showing the general  $(ABX_3)$  crystal structure of perovskite. In the case of  $\text{CH}_3\text{NH}_3\text{PbI}_3$ , A =  $\text{CH}_3\text{NH}_3$ , B = Pb, and X = I.

as hydrogen-bonding interactions between the hydrogens on the  $\text{NH}_3^+$  head and the iodide atoms.<sup>17,18</sup>

In this study, films of  $\text{CH}_3\text{NH}_3\text{PbI}_3$  perovskite were cast onto ca. 800 nm thick mesoporous  $\text{Al}_2\text{O}_3$  substrates (Figure SI-1 in the Supporting Information) from a 200 mg  $\text{mL}^{-1}$  solution of a 1:1 mol ratio  $\text{CH}_3\text{NH}_3\text{I}:\text{PbI}_2$  in DMF. The as-cast films were annealed at 70 °C for 30 min to form the crystalline perovskite structure. The  $\text{CH}_3\text{NH}_3\text{PbI}_3$  films exhibit a broad absorption across the visible range with two prominent peaks in the absorption spectra at approximately 750 and 490 nm. To identify the effects of humidity on the perovskite films, these films were stored in different humidity environments for an extended period. Figure 2A shows the UV-visible absorption spectra of  $\text{CH}_3\text{NH}_3\text{PbI}_3$  films stored in 90% RH in the dark for a period of 14 days. Over this relatively short time period there is a discoloration of the  $\text{CH}_3\text{NH}_3\text{PbI}_3$  from its original dark brown. Comparing the absorbance of the  $\text{CH}_3\text{NH}_3\text{PbI}_3$  film after 14 days to the absorbance of a pure  $\text{PbI}_2$  film, it is clear that, under the present conditions (viz. storage at room temperature in the dark), the films are not converted from  $\text{CH}_3\text{NH}_3\text{PbI}_3$  to  $\text{PbI}_2$ , as the decrease in absorbance of the  $\text{CH}_3\text{NH}_3\text{PbI}_3$  film occurs across the entire visible spectrum and not only wavelengths greater than 500 nm. This color change provides a facile means of detecting the perovskite film degradation.

To track the deterioration of the perovskite films stored in different humidity environments, we tracked the absorption of the film at 600 nm for films stored in 0%, 25%, 50%, and 90% RH at room temperature in the dark (Figure 2B). Humidity was controlled to approximately  $\pm 5\%$  by allowing equilibration with a mixture of glycerol and water.<sup>13</sup> The film stored at 0% humidity was kept in a sealed desiccator with fresh desiccant. Absorption measurements were taken in ambient conditions (typically  $\sim 50\%$  RH). While exposure to these conditions was kept to a minimum, this exposure likely had a small effect on those films stored at low humidity (viz., 0% and 25%). Over the course of the experiments, the temperature of the room was in the range of 22–24 °C. As seen in the case of the film stored at 90% RH, the absorbance of the film decays exponentially with time. By extrapolating the decay rate of the film absorbance, we can obtain an estimate of the time it takes for the perovskite film to decay to 50% of its initial absorbance value,  $t_{1/2}$ . Table 1 shows the estimated decay rate in terms of half-life,  $t_{1/2}$ , with increasing RH.

It is interesting to note that perovskite films undergo a faster decay when stored in light vs dark conditions, as shown in Figure SI-2 (Supporting Information). In addition, apart from

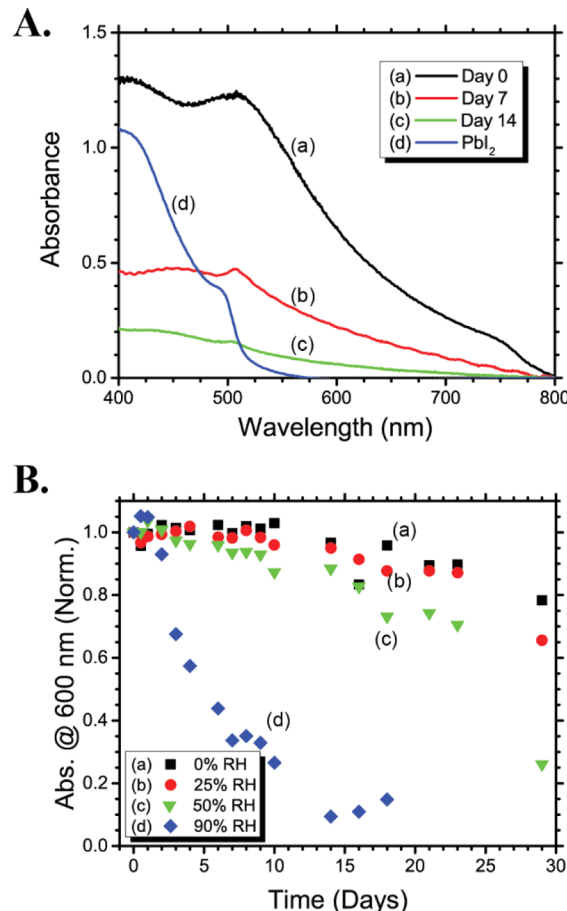


**Figure 2.** (A) UV-visible absorption spectra of (a) pristine perovskite film, films stored in the dark at room temperature in 90% relative humidity for (b) 7 and (c) 14 days, and (d) pristine  $\text{PbI}_2$  film. (B) Absorption at 600 nm of perovskite films stored in the dark at room temperature under (a) 0%, (b) 25%, (c) 50%, and (d) 90% relative humidity.

**Table 1. 50% Decay Time,  $t_{1/2}$ , of Perovskite Film Absorbance (600 nm) in Varying RH Environments**

% RH	$t_{1/2}$ (days)	% RH	$t_{1/2}$ (days)
0	76	50	26
25	57	90	4.6

the increased decay rate, the absorption spectra of perovskite films stored in the light show markedly different absorption features upon decay. The absorbance of films stored in the light ends up closely matching the absorbance of  $\text{PbI}_2$ , with a strong absorbance peak at 500 nm, as previously reported.<sup>11</sup> Previously reported crystallographic data obtained from  $\text{CH}_3\text{NH}_3\text{PbI}_3$  films which were degraded in the light confirmed that the perovskite films stored in the light do indeed eventually degrade to form  $\text{PbI}_2$ .<sup>10</sup> On the other hand, films that are kept in the dark display very low absorbance across the visible spectrum upon degradation and have only a weak absorption peak at 500 nm, as shown in Figure 2.

**Perovskite Film Morphology.** While the initial morphology of the film is important in the decay process,<sup>11</sup> exposure to a humid atmosphere can also significantly change the film morphology. We studied this change in morphology using scanning electron microscopy (SEM). For these experiments, perovskite films were deposited on top of a planar PEDOT

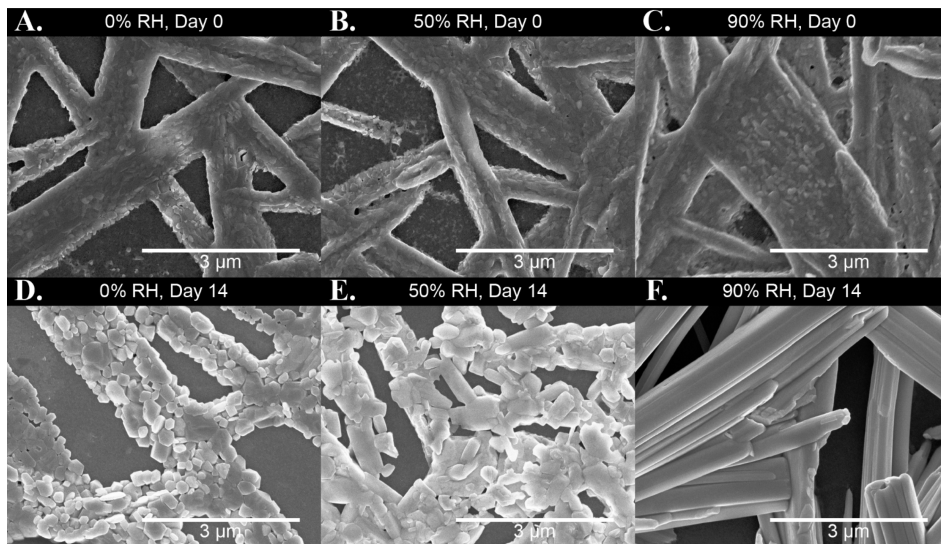


**Figure 3.** Scanning electron micrographs of perovskite films on planar PEDOT layers (i.e., no mesoporous scaffold) to highlight morphological changes undergone due to humidity exposure at room temperature in the dark. Images A–C were obtained immediately after perovskite deposition, while images D, E, and F were recorded after 14 days exposure in the dark to 0%, 50%, and 90% relative humidity, respectively.

layer so that changes in the perovskite structure could be clearly observed because the samples are not complicated by the presence of a mesoscopic support. In addition, PEDOT is more conductive than  $\text{Al}_2\text{O}_3$ , a critical difference necessary for obtaining high-resolution SEM images. This system is significantly different than the mesoporous  $\text{Al}_2\text{O}_3/\text{CH}_3\text{NH}_3\text{PbI}_3$  samples used, where the  $\text{CH}_3\text{NH}_3\text{PbI}_3$  is confined to nanometer-sized pores; however, this system may still allow for at least a qualitative understanding of the morphological changes in  $\text{CH}_3\text{NH}_3\text{PbI}_3$  induced by  $\text{H}_2\text{O}$  exposure. Figure 3 shows top-down scanning electron micrographs of films stored in 0%, 50%, and 90% RH for 14 days. These images reveal that, as the films age under these conditions, definite structural changes do occur. This is seen most clearly for the films that were stored at 90% RH. Before humidity exposure, all of the perovskite films have a somewhat rough surface, as seen in Figure 3A–C. However, after being in 90% RH for 14 days (Figure 3F), the perovskite undergoes a recrystallization process, becoming smooth and highly ordered. Films stored under 0% and 50% RH also show similar, though less severe, structural changes over this time period, exhibiting a coarsening of the perovskite (see parts D and E of Figure 3, respectively), similar to that reported for  $\text{CH}_3\text{NH}_3\text{PbI}_{3-x}\text{Cl}_x$  films stored under Ar.<sup>19</sup>

To better understand the effects of humidity on the perovskite structure and why such a distinct change occurs in both the absorption spectra and morphology of such films, XRD patterns were recorded. For these measurements, a 40 wt % solution of a 1:1 mol ratio  $\text{CH}_3\text{NH}_3\text{I}:\text{PbI}_2$  in DMF was cast onto the mesoporous  $\text{Al}_2\text{O}_3$  substrates in order to increase the signal-to-noise ratio. XRD patterns of (a) a  $\text{PbI}_2$  film on  $\text{Al}_2\text{O}_3$ , (b) a pristine  $\text{CH}_3\text{NH}_3\text{PbI}_3$  film on  $\text{Al}_2\text{O}_3$ , (c) an  $\text{Al}_2\text{O}_3/\text{CH}_3\text{NH}_3\text{PbI}_3$  film that had been stored under 50% RH for 28 days, (d) an  $\text{Al}_2\text{O}_3/\text{CH}_3\text{NH}_3\text{PbI}_3$  film stored under 90% RH for 7 days, and (e) synthesized  $(\text{CH}_3\text{NH}_3)_4\text{PbI}_6 \cdot 2\text{H}_2\text{O}$  crystals prepared using the methodology in ref 12. Characteristic XRD peaks are labeled on the figure for  $\text{PbI}_2$  (black square),  $\text{CH}_3\text{NH}_3\text{PbI}_3$  (red circle), and the  $\text{CH}_3\text{NH}_3\text{PbI}_3$  hydrate (green star).

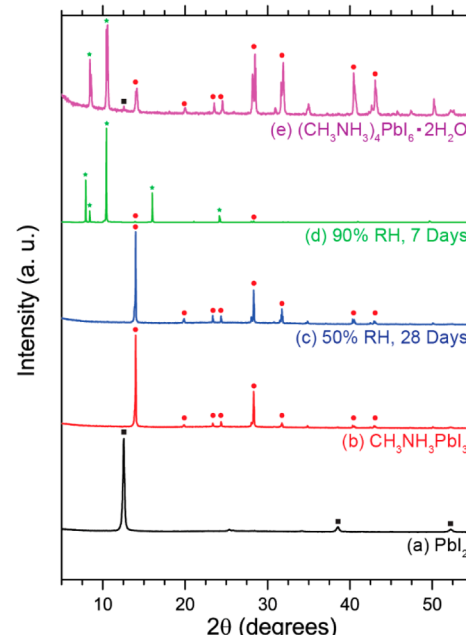
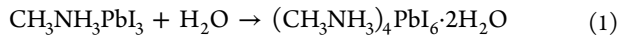


**Figure 4.** XRD patterns of (a)  $\text{PbI}_2$ , (b) a pristine  $\text{CH}_3\text{NH}_3\text{PbI}_3$  film, (c) a  $\text{CH}_3\text{NH}_3\text{PbI}_3$  film that has been stored at 50% RH in the dark for 28 days, (d) a  $\text{CH}_3\text{NH}_3\text{PbI}_3$  film that has been stored at 90% RH in the dark for 7 days, and (e)  $(\text{CH}_3\text{NH}_3)_4\text{PbI}_6 \cdot 2\text{H}_2\text{O}$  crystals prepared using the methodology in ref 12. Characteristic XRD peaks are labeled on the figure for  $\text{PbI}_2$  (black square),  $\text{CH}_3\text{NH}_3\text{PbI}_3$  (red circle), and the  $\text{CH}_3\text{NH}_3\text{PbI}_3$  hydrate (green star).

which arise due to reflections from the (110) and (220) crystal planes of the tetragonal perovskite structure at  $2\theta$  values of  $13.98^\circ$  and  $28.32^\circ$ , respectively.<sup>20</sup> There is no observable change in the XRD pattern between the pristine  $\text{CH}_3\text{NH}_3\text{PbI}_3$  film (b) and the  $\text{CH}_3\text{NH}_3\text{PbI}_3$  film after 28 days of storage at 50% relative humidity (c). To investigate the effects of high humidity exposure, a  $\text{CH}_3\text{NH}_3\text{PbI}_3$  film was stored under 90% RH for 7 days. As observed in Figure 2, these conditions cause a substantial lessening of film absorbance across the visible region. The XRD pattern also undergoes a major change from

that of  $\text{CH}_3\text{NH}_3\text{PbI}_3$ . Several new peaks arise at low angle that cannot be assigned to either  $\text{CH}_3\text{NH}_3\text{PbI}_3$  or  $\text{PbI}_2$ . Specifically, new peaks are seen at  $7.93^\circ$ ,  $8.42^\circ$ ,  $10.46^\circ$ , and  $16.01^\circ$ , but there still remain peaks visible at  $13.98^\circ$  and  $28.32^\circ$  that are attributed to crystalline  $\text{CH}_3\text{NH}_3\text{PbI}_3$  remaining in the film. Importantly, no peak is seen arising around  $12.55^\circ$ , which would evidence the presence of crystalline  $\text{PbI}_2$ .

We propose that upon exposure to humid air in the dark, a hydrate of  $\text{CH}_3\text{NH}_3\text{PbI}_3$  is formed (reaction 1).



Previously, Vincent et al. have characterized  $(\text{CH}_3\text{NH}_3)_4\text{PbI}_6 \cdot 2\text{H}_2\text{O}$ , a hydrate of  $\text{CH}_3\text{NH}_3\text{PbI}_3$ , which forms readily by the addition of aqueous  $\text{Pb}(\text{NO}_3)_2$  to an aqueous solution of  $\text{CH}_3\text{NH}_3\text{I}$ .<sup>12</sup> Formation of hydrate crystals in water can be visualized in the video presented in the Supporting Information. In contrast to the perovskite crystal structure of  $\text{CH}_3\text{NH}_3\text{PbI}_3$ , the crystal structure of  $(\text{CH}_3\text{NH}_3)_4\text{PbI}_6 \cdot 2\text{H}_2\text{O}$  consists of an assembly of  $\text{PbI}_6^{4-}$  octahedra and  $(\text{CH}_3\text{NH}_3 \cdots \text{H}_2\text{O} \cdots \text{H}_3\text{NH}_3\text{C})_2^{4+}$  dimers arranged on a distorted NaCl-type lattice.<sup>12</sup> This unique structure creates a zero-dimensional network of isolated  $\text{PbI}_6$  octahedra, as opposed to the extended three-dimensional network observed in  $\text{CH}_3\text{NH}_3\text{PbI}_3$ . Similar to the degraded perovskite films in the present experiments,  $(\text{CH}_3\text{NH}_3)_4\text{PbI}_6 \cdot 2\text{H}_2\text{O}$  is a pale yellow crystalline solid, and it has been suggested that the conversion from  $\text{CH}_3\text{NH}_3\text{PbI}_3$  to  $(\text{CH}_3\text{NH}_3)_4\text{PbI}_6 \cdot 2\text{H}_2\text{O}$  can occur in humid air.<sup>10</sup> Therefore, using XRD we investigated the possible link between the synthesized hydrate,  $(\text{CH}_3\text{NH}_3)_4\text{PbI}_6 \cdot 2\text{H}_2\text{O}$ , and the degraded perovskite films.

As shown in Figure 4 (spectrum e), the powder XRD pattern of synthesized hydrate crystals shows additional diffraction peaks associated with crystalline nonhydrated  $\text{CH}_3\text{NH}_3\text{PbI}_3$ . This  $\text{CH}_3\text{NH}_3\text{PbI}_3$  is formed as a result of the dehydration of as-prepared hydrate crystals while acquiring the XRD pattern. This facile dehydration and reversion to  $\text{CH}_3\text{NH}_3\text{PbI}_3$  was also observed by Vincent et al. in their previous work.<sup>12</sup> In fact, the crystals were seen to change color from their original pale yellow to black during the course of the measurement. Likewise, the degraded perovskite films recovered a portion of the perovskite absorbance upon storage in vacuum or low RH. This limited reversibility provides strong evidence for the formation of a  $\text{CH}_3\text{NH}_3\text{PbI}_3$  hydrate.

On comparing the XRD patterns of the two  $\text{CH}_3\text{NH}_3\text{PbI}_3$  hydrates [i.e., the degraded  $\text{CH}_3\text{NH}_3\text{PbI}_3$  film and the synthesized  $(\text{CH}_3\text{NH}_3)_4\text{PbI}_6 \cdot 2\text{H}_2\text{O}$  crystals], it is seen that both species have intense diffraction peaks at  $2\theta$  values of  $8.42^\circ$  and  $10.46^\circ$ , which suggests that both hydrates have the same structure. We are unable to irrefutably characterize the hydrate formed in either case as  $(\text{CH}_3\text{NH}_3)_4\text{PbI}_6 \cdot 2\text{H}_2\text{O}$  because the XRD patterns acquired do not directly correspond to the calculated powder XRD pattern of  $(\text{CH}_3\text{NH}_3)_4\text{PbI}_6 \cdot 2\text{H}_2\text{O}$  (PDF# 01-076-5812). Even so, we provisionally assign  $(\text{CH}_3\text{NH}_3)_4\text{PbI}_6 \cdot 2\text{H}_2\text{O}$  as the most probable hydrate species formed in the light of the precedent for the facile formation of  $(\text{CH}_3\text{NH}_3)_4\text{PbI}_6 \cdot 2\text{H}_2\text{O}$  crystals from aqueous solutions of  $\text{Pb}(\text{NO}_3)_2$  and  $\text{CH}_3\text{NH}_3\text{I}$ ; however, it is possible that additional hydrate forms of  $\text{CH}_3\text{NH}_3\text{PbI}_3$  other than  $(\text{CH}_3\text{NH}_3)_4\text{PbI}_6 \cdot 2\text{H}_2\text{O}$  appear following the humidity exposure.

**Charge Carrier Dynamics.** In addition to probing the ground-state absorption, we employed femtosecond transient absorption (TA) spectroscopy to examine the ultrafast dynamics of the photogenerated charge carriers in

$\text{CH}_3\text{NH}_3\text{PbI}_3$  films on  $\text{Al}_2\text{O}_3$ . The time-resolved absorption difference spectra of these films display three primary features, a strong band edge bleach at 750 nm that obeys clean second-order decay kinetics,<sup>21</sup> as well as a smaller bleach at 490 nm and an induced absorption centered at approximately 625 nm with distinctly different decay kinetics that together have been attributed to  $\text{PbI}_2$  impurities in the perovskite film<sup>22</sup> or a Pb–I charge transfer complex.<sup>23</sup> The evolution of the ground-state UV–visible absorption spectra and the TA spectra of a perovskite film stored at room temperature in the dark under 90% RH is shown in Figure 5. Similar plots for films stored under 0% and 50% RH are shown respectively in Figures SI-4 and SI-5 (Supporting Information). There is little change in the spectra during the initial stages of humidity exposure. However, beginning at day 7, another peak is seen at approximately 508 nm. This peak becomes more intense by day 10, while the perovskite peaks decrease in intensity, and by day 14, the 508 nm peak is the only peak visible as the perovskite features in the TA spectra are no longer observed. A similar behavior is observed over a longer time scale with films stored at 50% RH. This single sharp peak in the TA spectrum upon perovskite degradation is distinctly different from the TA spectrum of an unannealed film of 1:1 mol ratio  $\text{CH}_3\text{NH}_3\text{I}:\text{PbI}_2$ , while striking similarities exist between spectra recorded after day 14 (Figure 5F) and the TA spectrum of pure  $\text{PbI}_2$  (Figure SI-6, Supporting Information). While  $\text{CH}_3\text{NH}_3\text{PbI}_3$  films exposed to moisture in the light can form  $\text{PbI}_2$ ,<sup>10</sup> XRD measurements of humidity-degraded films in the dark do not reveal the presence of observable crystalline  $\text{PbI}_2$ . However, small quantities of  $\text{PbI}_2$  formed in the TA measurements (during laser exposure) can still elude XRD measurements.

The decay of the perovskite signal with exposure to humidity indicates that both the 490 nm bleach and the 750 nm band edge bleach observed in the present study are intrinsic to the perovskite itself, not the result of an impurity in the films. This is evidenced by the fact that throughout the experiment there is no significant change in the ratio between the 490 and 750 nm bleach peaks, as would be expected if the perovskite were only responsible for the 750 nm peak and the high energy bleach were contributed by a separate species. These observations strengthen the argument of our previous study that the high-energy bleach and induced absorption present in the transient absorption spectra of  $\text{CH}_3\text{NH}_3\text{PbI}_3$  are due to a charge-transfer excited state.<sup>23</sup>

Perhaps the most surprising finding of this study is observed when investigating the decay kinetics of the different features in the spectra. The kinetic decays in Figure 6 were assembled from the time-resolved spectral data taken at 0, 3, 7, and 10 days for the perovskite film stored under 90% RH. Despite changes in the film absorbance and morphology, there is essentially no change in the decay kinetics at any of the perovskite peaks (490, 625, or 750 nm). The changes in absorbance and morphology signal a significant modification of the surface of the  $\text{CH}_3\text{NH}_3\text{PbI}_3$  films, yet the absence of any change in decay kinetics over the 1.5 ns time window reveals that there is a limited contribution from trap-assisted recombination on this time scale. A similar absence of trap-assisted recombination has been previously observed in pristine perovskite films over these time scales,<sup>21,24</sup> meaning that despite the apparent surface changes, the perovskite excited state properties remain intact. This trend is very different than what is commonly seen in similar systems. For example, CdSe quantum dots that are exposed to oxygen exhibit a greatly

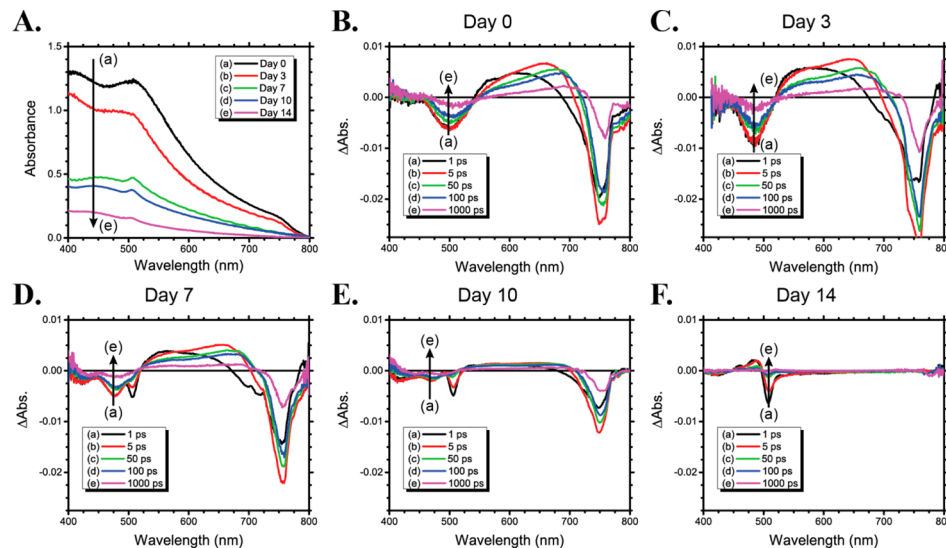


**Figure 5.** (A) UV–visible absorption spectra of  $\text{CH}_3\text{NH}_3\text{PbI}_3$  film stored at room temperature in the dark under 90% relative humidity for 0–14 days. Time-resolved absorption difference spectra after (B) 0 days, (C) 3 days, (D) 7 days, (E) 10 days, and (F) 14 days under these conditions.

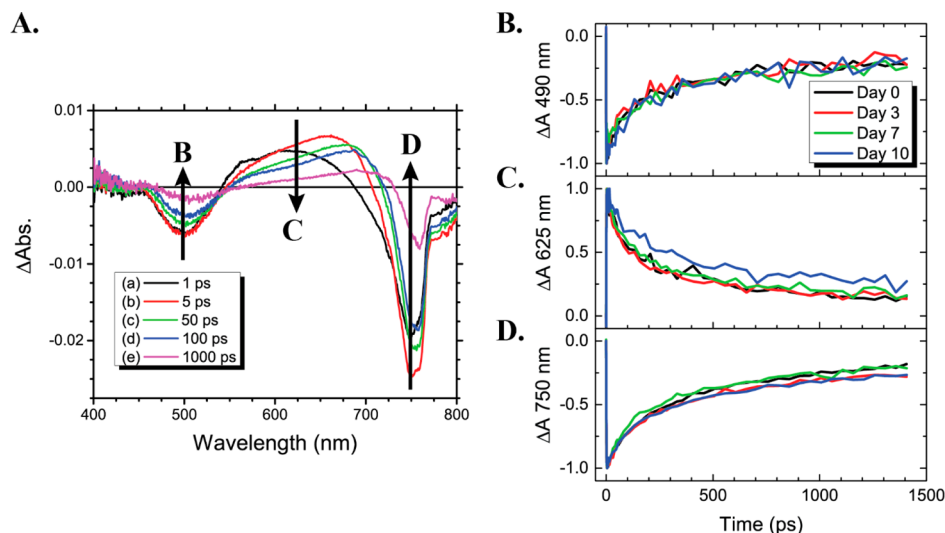


**Figure 6.** (A) Representative femtosecond transient absorption spectra of the perovskite film showing wavelengths at which the recovery kinetics were probed. Time-resolved kinetic traces assembled at (B) 490 nm, (C), 625 nm, and (D) 760 nm for a perovskite film stored between 0 and 10 days at 90% RH at room temperature in the dark.

reduced excited state lifetime because the oxidation process induces the formation of trap states, which can then act as recombination centers.<sup>25</sup>

**Humidity Effects on Photovoltaic Performance.** We next observed the effect of humidity on the performance of  $\text{TiO}_2/\text{CH}_3\text{NH}_3\text{PbI}_3/\text{spiro-OMeTAD}$  solar cells. The procedure for making the perovskite solar cells was adapted from one originally developed by Park and co-workers.<sup>26</sup> The perovskite films were deposited by a two-step spin-coating technique onto a 150 nm thick mesoporous  $\text{TiO}_2$  scaffold (ca. 40 nm  $\text{TiO}_2$  particles). A spiro-OMeTAD hole conductor layer was cast on top of the perovskite films, and the solar cell was completed by evaporation of a 100 nm gold contact. The solar cells were not encapsulated after Au deposition. A cross sectional SEM image of a completed device is shown in Figure SI-7 (Supporting Information).

Photoelectrochemical performance of these devices was measured under 100 mW  $\text{cm}^{-2}$  AM1.5 simulated solar

irradiation in ambient conditions (RH ~ 50%). The current–voltage characteristics of the champion device are presented in Figure 7A. This solar cell displayed a short-circuit current of 20.6 mA  $\text{cm}^{-2}$ , an open-circuit voltage of 1.008 V, a fill factor of 0.63, and a power conversion efficiency of 13.1%. As discussed in several recent papers, it is important to characterize the performance of perovskite solar cells beyond just a simple  $J$ – $V$  curve due to both  $J$ – $V$  hysteresis and the rapid degradation of some devices.<sup>27,28</sup> Therefore, we performed an in depth characterization of the photovoltaic performance of a representative device in order to confirm the accuracy of the reported  $J$ – $V$  curves. As shown in Figure-SI-8 (Supporting Information), there is good agreement between the short-circuit photocurrent measured in the  $J$ – $V$  curves under the experimental conditions and the integrated incident photon to current efficiency (IPCE). Also, there is a close matching between the power conversion efficiency obtained from the maximum point on the  $J$ – $V$  curve and the stabilized efficiency

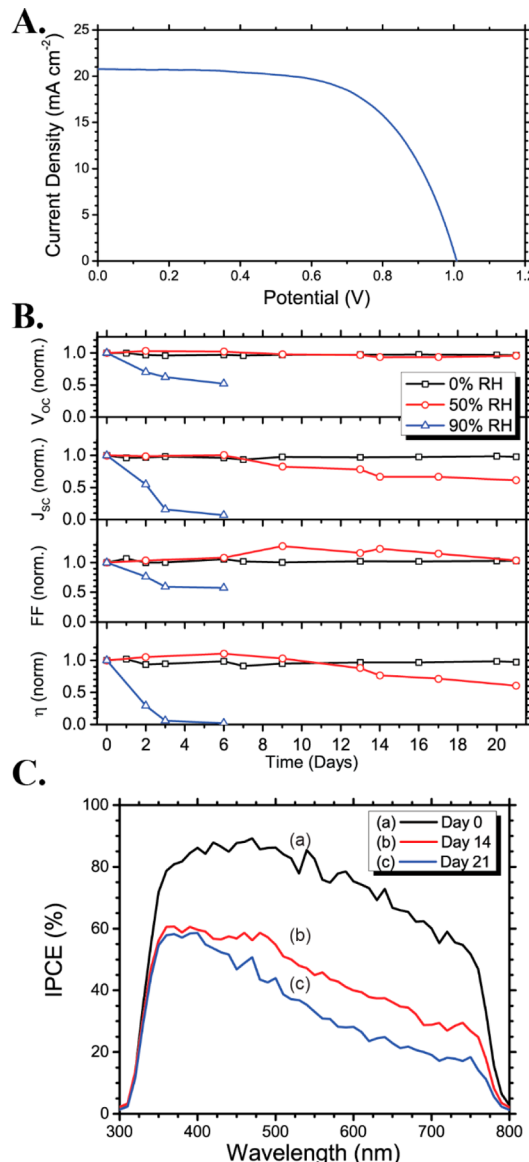


**Figure 7.** (A) Current–voltage characteristics of champion  $\text{TiO}_2/\text{CH}_3\text{NH}_3\text{PbI}_3/\text{spiro-OMeTAD}$  solar cell under  $100 \text{ mW cm}^{-2}$  AM 1.5 irradiation. The scan was taken with a scan rate of  $200 \text{ mV s}^{-1}$  from forward bias to short-circuit conditions. The active area of the solar cell was masked and the area measured to be  $0.113 \text{ cm}^2$ . (B) Stacked plot of the normalized performance parameters with time for solar cells from Table 2 stored in 0%, 50%, and 90% RH. (C) IPCE spectra of perovskite solar cell that was stored in 50% RH taken following exposure to these conditions for (a) 0 days, (b) 14 days, and (c) 21 days.

determined by monitoring the photocurrent while the cell potential is held at its maximum power point for 120 s. These measurements corroborate the reported PV parameters and witness to the accuracy of the measured  $J$ – $V$  curves.

The stability of these solar cells was tested in three different controlled humidity environments, 0%, 50%, and 90% RH. Three devices were selected that had been fabricated as part of the same batch of solar cells and displayed largely similar  $J$ – $V$  characteristics (Table 2). The solar cells were then stored under these conditions in the dark without encapsulation. The evolution of their performance characteristics was monitored over the course of 21 days. In a typical experiment, the solar

**Table 2.** Initial  $J$ – $V$  Characteristics of Perovskite Solar Cells That Were Subsequently Stored at the Stated Relative Humidity

% RH	$J_{\text{SC}}$ ( $\text{mA cm}^{-2}$ )	$V_{\text{OC}}$ (V)	FF	$\eta$ (%)
90	19.5	1.022	0.61	12.1
0	20.6	1.008	0.63	13.1
50	17.4	0.993	0.61	10.6

cells were measured using rapid current–voltage scans (typical scan rate  $200 \text{ mV s}^{-1}$ ) in order to minimize the potential for performance degradation due to extended illumination and testing in ambient atmosphere. The PV parameters obtained from these measurements (viz.,  $J_{\text{SC}}$ ,  $V_{\text{OC}}$ , FF, and  $\eta$ ) were normalized to the initial value and the normalized values were plotted over the course of the experiment (Figure 7B).

The solar cell stored under 90% RH underwent a rapid decrease in PV performance from initially over 12% to less than 1% efficiency in only 3 days (day 3:  $J_{\text{SC}} = 3.1 \text{ mA cm}^{-2}$ ,  $V_{\text{OC}} = 0.637$ , FF = 0.36,  $\eta$  = 0.7%). Degradation in PV performance was much less precipitous for the solar cells stored at 50% RH and 0% RH. For those stored in dry conditions, very little change in the  $J$ – $V$  curve was observed over the course of the 21 days. This solar cell saw the efficiency decline from 13.1% initially to 12.8% over this time span, a loss of less than 5%. A majority of this decline in performance was due to the lower  $V_{\text{OC}}$  which dropped from 1.008 to 0.971 V over the 21 days.

In the case of the solar cell stored at 50% RH, a reduction in power conversion efficiency of approximately 40% took place over the course of the 21 day experiment. Unlike the case of the solar cell held in dry air, the majority of the decay occurred because of the  $J_{\text{SC}}$ , which fell from  $17.4 \text{ mA cm}^{-2}$  to just  $10.6 \text{ mA cm}^{-2}$ . The fill factor actually underwent an increase over the first days of testing from 0.61 to 0.78 at day 9, although this rise is attributed to the larger hysteresis observed in the  $J$ – $V$  curves upon humidity exposure (Figure SI-9, Supporting Information), which decreases the confidence in the resultant PV parameters. This also necessitated using a slower scan rate ( $25 \text{ mV s}^{-1}$ ) to obtain a more accurate  $J$ – $V$  curve as the humidity degradation progressed. Figure SI-10 (Supporting Information) shows the  $J$ – $V$  curves, stabilized power conversion efficiency, and IPCE spectra of the solar cells after exposure to 0% and 50% RH for 21 days. It should be noted that the stabilized power conversion efficiency does not match the efficiency measured from the  $J$ – $V$  curve as accurately at the end of the experiment as at the beginning (Figure SI-10B, Supporting Information), and the stabilized power conversion efficiency for the cells stored at 0% and 50% RH for 21 days displays slightly lower stability than initially.

Incident photon to current efficiency (IPCE) was measured for the solar cell stored at 50% RH several times over the course of the experiment to further investigate the reason for the lower power conversion efficiency. Initially, the IPCE spectra shows very high quantum efficiencies across the entire visible spectra with a peak external quantum efficiency (EQE) of  $\sim 85\%$  between 400 and 500 nm. As shown in Figure 7C, the IPCE stayed relatively high in the blue portion of the solar spectrum, with a peak EQE of nearly 60%, but decreased much more rapidly in the red region from 60% at 700 nm initially to 19% after the 21 day exposure.

## CONCLUSIONS

When exposed to humid air in the dark,  $\text{CH}_3\text{NH}_3\text{PbI}_3$  does not merely revert to  $\text{PbI}_2$  with a loss of  $\text{CH}_3\text{NH}_3\text{I}$ , as has been postulated for  $\text{CH}_3\text{NH}_3\text{PbI}_3$  films at temperature in the light.<sup>10</sup> We now have evidence for the formation of a  $\text{CH}_3\text{NH}_3\text{PbI}_3$  hydrate that has similarities to the previously characterized hydrate  $(\text{CH}_3\text{NH}_3)_4\text{PbI}_6 \cdot 2\text{H}_2\text{O}$ . This is evidenced by the crystal structure and optical properties of the degraded perovskite material compared to those of  $\text{PbI}_2$  as well as  $(\text{CH}_3\text{NH}_3)_4\text{PbI}_6 \cdot 2\text{H}_2\text{O}$ . The incorporation of  $\text{H}_2\text{O}$  leads to a loss in absorbance across the visible spectrum similar to that seen previously by Zhao and Zhu when perovskite films were exposed to ammonia vapor.<sup>29</sup> In this previous study as well, when  $\text{CH}_3\text{NH}_3\text{PbI}_3$  is exposed to  $\text{NH}_3$  vapor, a structural and optical change occurs wherein the perovskite film turns from dark brown/black to colorless. As with the case of long ammonia exposure (tens of minutes), we do not observe a complete recovery of the perovskite structure upon removal of the  $\text{H}_2\text{O}$  vapor; however, partial recovery does occur.

While significant changes are seen in the UV-visible absorbance, the presence of the hydrate in the films has no noticeable effect on the charge carrier dynamics at short times (<1.5 ns). This is surprising considering the large carrier diffusion lengths in  $\text{CH}_3\text{NH}_3\text{PbI}_3$  and the pervasiveness of trap-state-mediated recombination in semiconductor systems.<sup>25,30,34,35</sup> Nevertheless, this can be rationalized due to the unique defect physics of  $\text{CH}_3\text{NH}_3\text{PbI}_3$ . Previous studies have shown by calculation and experiment that defects in the  $\text{CH}_3\text{NH}_3\text{PbI}_3$  crystal lattice form only shallow trap states, while trap-mediated recombination mechanisms are essentially absent on the nanosecond time scale.<sup>21,24,31–33</sup> These previous observations explain the long carrier diffusion lengths of these solution-processed films and also serve to clarify the effect seen in the present work. It is proposed that  $\text{H}_2\text{O}$  initially reacts with the surface of the perovskite film and only slowly permeates through to the center of large domains. The reaction with  $\text{H}_2\text{O}$  at the surface of the perovskite film forms shallow traps in the band structure, so that the portion of the  $\text{CH}_3\text{NH}_3\text{PbI}_3$  crystal which is pristine remains largely unaffected. This gives rise to the behavior shown in Figures 5 and 6, where the ultrafast excited state kinetics and the photobleaching peak positions remain unchanged despite the film having undergone near total degradation.

PV performance of perovskite solar cells was seen to decrease much more rapidly than the UV-visible absorption and excited state characteristics of the  $\text{CH}_3\text{NH}_3\text{PbI}_3$  films. While a bare  $\text{CH}_3\text{NH}_3\text{PbI}_3$  film exposed to 90% RH for 3 days saw only a marginal decrease in absorbance and no change in excited state dynamics on the picosecond time-scale, the efficiency of a  $\text{CH}_3\text{NH}_3\text{PbI}_3/\text{spiro-OMeTAD}$  solar cell stored under the same conditions decreased nearly 95% over the same time period in spite of the spiro-OMeTAD layer protecting the  $\text{CH}_3\text{NH}_3\text{PbI}_3$  film from moisture.<sup>10</sup> This points to a breakdown of long-range charge transport and/or a deleterious modification of the  $\text{CH}_3\text{NH}_3\text{PbI}_3/\text{spiro-OMeTAD}$  interface, and not to absolute changes in the perovskite excited state or optical absorption, as the primary mechanism responsible for the loss of PV performance.

In the perovskite crystals,  $\text{CH}_3\text{NH}_3^+$  is bound to the  $\text{PbI}_6$  octahedra by hydrogen-bonding interactions. Even when not illuminated, the  $\text{CH}_3\text{NH}_3^+$  cations exhibit a dynamic disorder in the room temperature tetragonal perovskite phase,<sup>36</sup> while the

charge transfer nature of the  $\text{CH}_3\text{NH}_3\text{PbI}_3$  band gap causes the  $\text{CH}_3\text{NH}_3^+$  ions to be less tightly bound after photoexcitation than they are in the ground state.<sup>37</sup> From this, we hypothesize that the observed hydration of  $\text{CH}_3\text{NH}_3\text{PbI}_3$  likely occurs when  $\text{H}_2\text{O}$  forms a stronger hydrogen-bonding interaction than that formed by  $\text{CH}_3\text{NH}_3^+$ . The fact that the degradation processes occur more rapidly upon illumination, when the  $\text{CH}_3\text{NH}_3^+$  hydrogen-bonding strength is lessened, supports this hypothesis, as does the reported structure of  $(\text{CH}_3\text{NH}_3)_4\text{PbI}_6 \cdot 2\text{H}_2\text{O}$ .<sup>12</sup> This suggests that strengthening the hydrogen-bonding interaction between the organic cation and metal halide octahedra and/or weakening the hydrogen interaction between the organic cation and  $\text{H}_2\text{O}$  could improve moisture resistance, making this a promising area for further work toward developing commercial perovskite solar cells.

## ASSOCIATED CONTENT

### S Supporting Information

SEM cross section images of  $\text{Al}_2\text{O}_3$  films and photovoltaic device, control XRD and femtosecond transient absorption experiments, detailed analysis of photovoltaic device performance characteristics, and video showing the formation of the  $\text{CH}_3\text{NH}_3\text{PbI}_3$  hydrate. This material is available free of charge via the Internet at <http://pubs.acs.org>.

## AUTHOR INFORMATION

### Corresponding Author

pkamat@nd.edu

### Notes

The authors declare no competing financial interest.

## ACKNOWLEDGMENTS

This work was supported by the Division of Chemical Sciences, Geosciences, and Biosciences, Office of Basic Energy Sciences of the U.S. Department of Energy through award DE-FC02-04ER15533. J.A.C. acknowledges support from the Jana & Patrick Eilers Energy Research Fellowship administered through the center for Sustainable Energy and Notre Dame (cSEND), and the Bayer Predoctoral Research Fellowship administered through the Center for Environmental Science and Technology (CEST). P.A.M.H. acknowledges the support of the University of Notre Dame through the iSURE undergraduate fellowship program. The authors thank the cSEND Materials Characterization Facility for the use of the Bruker pXRD. The authors would also like to thank Dr. Julie Peller and Joseph Manser, for fruitful discussions, and Dr. Nam-Gyu Park and his research group, for their generous gift of the  $\text{TiO}_2$  paste used for PV fabrication. This is contribution number NDRL No. 5047 from the Notre Dame Radiation Laboratory.

## REFERENCES

- (1) Green, M. A.; Emery, K.; Hishikawa, Y.; Warta, W.; Dunlop, E. D. *Prog. Photovoltaics Res. Appl.* **2014**, *22*, 701–710.
- (2) Eperon, G. E.; Burlakov, V. M.; Goriely, A.; Snaith, H. J. *ACS Nano* **2014**, *8*, 591–598.
- (3) Park, N. *J. Phys. Chem. Lett.* **2013**, *4*, 2423–2429.
- (4) Green, M. A.; Ho-Baillie, A.; Snaith, H. J. *Nat. Photonics* **2014**, *8*, 506–514.
- (5) Christians, J. A.; Fung, R. C. M.; Kamat, P. V. *J. Am. Chem. Soc.* **2014**, *136*, 758–764.
- (6) Leijtens, T.; Eperon, G. E.; Pathak, S.; Abate, A.; Lee, M. M.; Snaith, H. J. *Nat. Commun.* **2013**, *4*, 2885.

- (7) Noh, J. H.; Im, S. H.; Heo, J. H.; Mandal, T. N.; Seok, S. I. *Nano Lett.* **2013**, *13*, 1764–1769.
- (8) Zhou, H.; Chen, Q.; Li, G.; Luo, S.; Song, T.-B.; Duan, H.-S.; Hong, Z.; You, J.; Liu, Y.; Yang, Y. *Science* **2014**, *345*, 542–546.
- (9) Bass, K. K.; McAnally, R. E.; Zhou, S.; Djurovich, P. I.; Thompson, M.; Melot, B. *Chem. Commun.* **2014**, *50*, 15819–15822.
- (10) Habisreutinger, S. N.; Leijtens, T.; Eperon, G. E.; Stranks, S. D.; Nicholas, R. J.; Snaith, H. J. *Nano Lett.* **2014**, *14*, 5561–5568.
- (11) Smith, I. C.; Hoke, E. T.; Solis-Ibarra, D.; McGhee, M. D.; Karunadasa, H. I. *Angew. Chem.* **2014**, *126*, 11414–11417.
- (12) Vincent, B. R.; Robertson, K. N.; Cameron, T. S.; Knop, O. *Can. J. Chem.* **1987**, *65*, 1042–1046.
- (13) Forney, C. F.; Brandl, D. G. *HortTechnology* **1992**, *2*, 52–54.
- (14) Lee, J.-W.; Lee, T.-Y.; Yoo, P. J.; Grätzel, M.; Mhaisalkar, S.; Park, N.-G. *J. Mater. Chem. A* **2014**, *2*, 9251–9259.
- (15) Burschka, J.; Pellet, N.; Moon, S.-J.; Humphry-Baker, R.; Gao, P.; Nazeeruddin, M. K.; Grätzel, M. *Nature* **2013**, *499*, 316–319.
- (16) Noel, N. K.; Stranks, S. D.; Abate, A.; Wehrenfennig, C.; Guarnera, S.; Haghhighirad, A.; Sadhanala, A.; Eperon, G. E.; Pathak, S. K.; Johnston, M. B.; Petrozza, A.; Herz, L.; Snaith, H. *Energy Environ. Sci.* **2014**, *7*, 3061–3068.
- (17) Mitzi, D. B.; Dimitrakopoulos, C. D.; Kosbar, L. L. *Chem. Mater.* **2001**, *13*, 3728–3740.
- (18) Quarti, C.; Grancini, G.; Mosconi, E.; Bruno, P.; Ball, J. M.; Lee, M. M.; Snaith, H. J.; Petrozza, A.; Angelis, F. De. *J. Phys. Chem. Lett.* **2014**, *5*, 279–284.
- (19) Park, B.; Johansson, E. M. J.; Philippe, B.; Gustafsson, T.; Sveinbjörnsson, K.; Hagfeldt, A.; Boschloo, G. *Chem. Mater.* **2014**, *26*, 4466–4471.
- (20) Zhao, Y.; Zhu, K. *J. Phys. Chem. Lett.* **2013**, *4*, 2880–2884.
- (21) Manser, J. S.; Kamat, P. V. *Nat. Photonics* **2014**, *8*, 737–743.
- (22) Wang, L.; McCleese, C.; Kovalsky, A.; Zhao, Y.; Burda, C. *J. Am. Chem. Soc.* **2014**, *136*, 12205–12208.
- (23) Stamplecoskie, K. G.; Manser, J. S.; Kamat, P. V. *Energy Environ. Sci.* **2015**, *8*, 208–215.
- (24) Wehrenfennig, C.; Eperon, G. E.; Johnston, M. B.; Snaith, H. J.; Herz, L. M. *Adv. Mater.* **2014**, *26*, 1584–1589.
- (25) Hines, D. A.; Becker, M. A.; Kamat, P. V. *J. Phys. Chem. C* **2012**, *116*, 13452–13457.
- (26) Luo, J.; Im, J.-H.; Mayer, M. T.; Schreier, M.; Nazeeruddin, M. K.; Park, N.-G.; Tilley, S. D.; Fan, H. J.; Gratzel, M. *Science* **2014**, *345*, 1593–1596.
- (27) Snaith, H. J.; Abate, A.; Ball, J. M.; Eperon, G. E.; Leijtens, T.; Noel, N. K.; Stranks, S. D.; Wang, J. T.-W.; Wojciechowski, K.; Zhang, W. *J. Phys. Chem. Lett.* **2014**, *5*, 1511–1515.
- (28) Zimmermann, E.; Ehrenreich, P.; Pfadler, T.; Dorman, J. A.; Weickert, J.; Schmidt-Mende, L. *Nat. Photonics* **2014**, *8*, 669–672.
- (29) Zhao, Y.; Zhu, K. *Chem. Commun. (Cambridge, U. K.)* **2014**, *50*, 1605–1607.
- (30) Christians, J. A.; Kamat, P. V. *ACS Nano* **2013**, *7*, 7967–7974.
- (31) Yin, W.-J.; Shi, T.; Yan, Y. *Appl. Phys. Lett.* **2014**, *104*, 063903.
- (32) Edri, E.; Kirmayer, S.; Henning, A.; Mukhopadhyay, S.; Gartsman, K.; Rosenwaks, Y.; Hodes, G.; Cahen, D. *Nano Lett.* **2014**, *14*, 1000–1004.
- (33) Oga, H.; Saeki, A.; Ogomi, Y.; Hayase, S.; Seki, S. *J. Am. Chem. Soc.* **2014**, *136*, 13818–13825.
- (34) Xing, G.; Mathews, N.; Sun, S.; Lim, S. S.; Lam, Y. M.; Gratzel, M.; Mhaisalkar, S.; Sum, T. C. *Science* **2013**, *342*, 344–347.
- (35) Stranks, S. D.; Eperon, G. E.; Grancini, G.; Menelaou, C.; Alcocer, M. J. P.; Leijtens, T.; Herz, L. M.; Petrozza, A.; Snaith, H. J. *Science* **2013**, *342*, 341–344.
- (36) Poglitsch, A.; Weber, D. *J. Chem. Phys.* **1987**, *87*, 6373–6378.
- (37) Gottesman, R.; Haltzi, E.; Gouda, L.; Tirosh, S.; Bouhadana, Y.; Zaban, A.; Mosconi, E.; De Angelis, F. *J. Phys. Chem. Lett.* **2014**, *5*, 2662–2669.